

INTERACTION OF LASER RADIATION WITH MATTER. LASER PLASMA https://doi.org/10.1070/QEL16290

Experimental capabilities of the GARPUN MTW Ti:sapphire–KrF laser facility for investigating the interaction of subpicosecond UV pulses with targets*

V.D. Zvorykin, S.A. Goncharov, A.A. Ionin, D.V. Mokrousova, S.V. Ryabchuk, L.V. Seleznev, E.S. Sunchugasheva, N.N. Ustinovskii, A.V. Shutov

Abstract. **This paper describes the first experiments carried out on the GARPUN MTW Ti:sapphire–KrF hybrid laser facility and aimed at gaining insight into the interaction of subpicosecond UV pulses with solid and structured low-density carbon nanotube targets at peak intensities of $\sim 10^{16}$ W cm^{-2} in a focal spot $\sim$70 μm in size. Using X-ray absorbers, the plasma electron temperature has been measured to be ~850 eV. In our experiments, we used an optimal configuration: direct double-pass ultrashort-pulse (USP) amplification in KrF amplifier stages, with multiple laser beam filamentation suppression in a xenon-filled cell. The highest energy on a target was 0.25 J at a USP contrast relative to amplified spontaneous emission of $\sim 3\times 10^{10}$ for intensities and $\sim 3\times 10^{5}$ for fluences. Owing to two-photon resonance in the UV spectral region, the use of xenon, with a negative nonlinear refractive index, allowed us to make the cross-sectional fluence distribution more uniform and reduce the beam divergence to 0.14 mrad (at the 10% intensity level). Reducing the USP duration via negatively chirped pulse amplification and filamentation suppression and reducing the focal spot size on a target by using parabolic short-focus optics are expected to ensure an increase in the intensity incident on the target by one to two orders of magnitude.**

Keywords: *amplification of subpicosecond terawatt pulses in KrF amplifiers, interaction of intense UV pulses with targets.*

1. Introduction

The last two decades have seen rapid advances in solid-state laser systems with frequency-chirped near-IR pulse amplification. They have ensured record high peak powers of femto- and picosecond pulses, at a level of 1 PW (see a review by Danson et al. [1]). Spectral and temporal transformations of ultrashort pulses (USPs) before amplification and subsequent compression of the stretched pulses to their original duration have made it possible to suppress laser beam self-focusing in solid-state amplifiers. At present, such systems are used in the vast majority of experiments concerned with the interaction of IR radiation with targets at ultrahigh intensities (up to $\sim 10^{22}$ W cm^{-2}): acceleration of charged particles in a laser plasma, research into the physics of high energy densities, laboratory simulation of astrophysical phenomena, laser fusion, etc. A viable alternative to solid-state chirped pulse amplification systems is KrF laser systems, which were thought in the 1990s to have a great future (see [2, 3] and references therein). In KrF laser amplifiers, direct amplification of transform-limited UV USPs at a wavelength $\lambda = 248$ nm is possible, because the gaseous gain medium has a three to four orders of magnitude smaller Kerr nonlinearity coefficient n_2, which is responsible for self-focusing. In particular, the Super-Sprite [4, 5] and Super-Ashura [6] laser facilities, which took advantage of electron beam-pumped large-aperture KrF amplifiers, ensured picosecond pulse energies up to ~10 J, with peak powers as high as 10 TW and focused beam intensities reaching 10^{20} W cm^{-2}.

Wide use was also made of compact repetitively pulsed laser systems where USPs were amplified by discharge-pumped KrF amplifiers, which provided pulse energies of tens and hundreds of millijoules at shorter, subpicosecond pulse durations [7–12]. Such systems were used to carry out a variety of experiments on the interaction of UV USPs with targets at intensities up to 10^{17} W cm^{-2} and a focal spot size of ~10 μm. The experiments were aimed at producing quasi-continuous coherent and incoherent VUV and soft X-ray sources via the generation of high harmonics and dense laser plasma radiation [13–33].

Even though KrF laser systems generating USPs are at present inferior in many parameters to solid-state lasers, they have some important advantages from the viewpoint of interaction with matter, related primarily to their short emission wavelength and the possibility of generating a train of USPs with a nanosecond pulse separation or varying the temporal pulse profile on a target. Since the critical electron plasma density increases with decreasing wavelength as $n_{ecr} \propto \lambda^{-2}$, a UV USP penetrates deeper into a laser plasma, producing a higher pressure in a dense plasma. This is of paramount importance for laser fusion. After the failure to obtain a fusion energy comparable to the laser pulse energy in the indirect-drive approach at the NIF, the world's largest solid-state

* Presented at the ECLIM 2016 conference (Moscow, 18–23 September 2016.

V.D. Zvorykin P.N. Lebedev Physics Institute, Russian Academy of Sciences, Leninsky prosp. 53, 119991 Moscow, Russia; National Research Nuclear University 'MEPhI', Kashirskoe sh. 31, 115409 Moscow, Russia; e-mail: zvorykin@sci.lebedev.ru;
S.A. Goncharov, S.V. Ryabchuk National Research Nuclear University 'MEPhI', Kashirskoe sh. 31, 115409 Moscow, Russia;
A.A. Ionin, L.V. Seleznev, E.S. Sunchugasheva, N.N. Ustinovskii, A.V. Shutov P.N. Lebedev Physics Institute, Russian Academy of Sciences, Leninsky prosp. 53, 119991 Moscow, Russia;
D.V. Mokrousova P.N. Lebedev Physics Institute, Russian Academy of Sciences, Leninsky prosp. 53, 119991 Moscow, Russia; Moscow Institute of Physics and Technology (State University), Institutskii per. 9, 141701 Dolgoprudnyi, Moscow region, Russia

Received 24 January 2017; revision received 22 February 2017
Kvantovaya Elektronika **47** (4) 319–326 (2017)
Translated by O.M. Tsarev

laser facility in the United States, KrF lasers again attracted researchers' attention, in particular in the context of 'shock ignition', a promising approach in which a target is exposed to a laser pulse with a sharp rise in its intensity to 10^{16} W cm^{-2} at the end of the pulse [34]. Pulse shaping can be achieved by exposing a target to a combination of long (nanosecond) and short (picosecond) pulses in an angular multiplexing scheme [35]. In this process, both types of pulses can be simultaneously amplified in the same KrF amplifier stages, because the population inversion in their gain medium becomes restored in a short time (~2 ns) [2, 36]. In addition, UV USPs have an advantage over IR radiation from solid-state lasers in new schemes for accelerating charged particles (electrons and protons) in laser plasmas generated by low-density targets [37].

This paper describes the experimental capabilities of the GARPUN MTW Ti:sapphire–KrF laser facility for investigating the interaction of terawatt peak power, subpicosecond UV pulses with targets. We substantiate the choice of direct double-pass USP amplification in KrF amplifier stages with the aim of maximising the output power, USP contrast, laser beam quality and, hence, the laser intensity incident on a target and examine the effects of multiple laser beam filamentation and filamentation suppression due to the Kerr defocusing of the filaments in xenon on the beam divergence. The results of the first experiments on the interaction of UV USPs with various targets at intensities of ~10^{16} W cm^{-2} are presented.

2. GARPUN MTW Ti:sapphire–KrF laser facility

Our experimental studies were carried out at the GARPUN MTW Ti:sapphire–KrF hybrid laser facility, which was described in detail previously [2]. The laser facility comprises two electron beam-pumped KrF amplifier stages (GARPUN final large-aperture amplifier with a gain medium 12×18×100 cm in dimensions and 8×8×110-cm Berdysh preamplifier), a discharge-pumped KrF laser (Lambda Physik EMG Model TMSC 150) for synchronising the pumping of the amplifiers (igniting the dischargers of the pulsed high-voltage power supply system of electron accelerators) and a Start-248M Ti:sapphire front-end (Avesta Project Ltd.), whose output is frequency-tripled in nonlinear crystals. After front-end frequency conversion to the KrF gain band, the UV USP energy reaches 0.5 mJ at a pulse duration of ~100 fs. To control the synchronisation of USPs with the pumping of the KrF amplifiers, we use vacuum photodiodes placed near the preamplifier and final amplifier (see the schematic of the experimental setup in Fig. 1). The photodiodes simultaneously detect a USP and the amplified spontaneous emission (ASE) pulse reproducing the electron beam pump pulse.

Optimising direct USP amplification in the large-aperture KrF amplifier stages in order to maximise the output pulse energy at the minimum possible ASE energy and shortest possible USP duration, we chose double-pass USP amplification in the preamplifier and final amplifier [38]. The highest energy of USPs amplified in this configuration reached 0.6 J at a pulse duration under 1 ps, which was determined by the dispersion-induced pulse broadening in the windows of the amplifiers and along the extended air path of ~50 m length [39]. In this way, we have reached terawatt USP peak powers. Moreover, we have demonstrated the amplification of trains of subterawatt USPs with a repetition period of a few nanoseconds [38], as well as simultaneous amplification of a train of USPs and a long pulse of 100 ns duration [40].

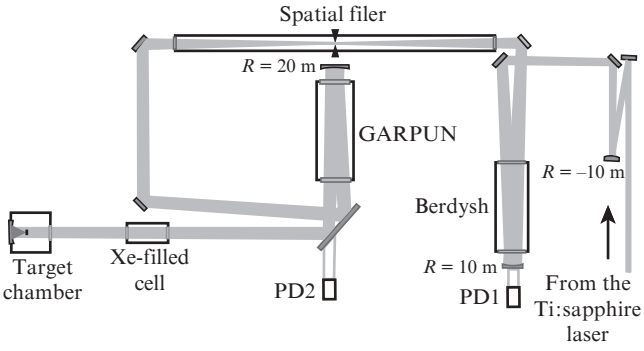

Figure 1. Schematic of double-pass USP amplification in the KrF amplifiers and pulse delivery to the target chamber (R is the radius of curvature of the mirrors).

3. Multiple filamentation of a UV laser beam and filamentation suppression in xenon

3.1. Effect of filamentation on USP energy saturation

The critical power for UV light self-focusing is $P_{cr} \approx 0.1$ GW, which is four orders of magnitude lower than the amplified USP peak power P obtained to date. At $P \gg P_{cr}$, the laser beam becomes unstable and breaks up into many small light filaments over a long amplification path [39, 41, 42]. The peak light intensity I_f and peak fluence ε_f in filaments are ~0.2 TW cm^{-2} and ~0.2 J cm^{-2}, respectively. With allowance for background radiation, these values are 200 times the respective cross-section averages. Note that ε_f is five to ten times higher than the maximum possible USP fluence in KrF as a gain medium: $\varepsilon_{lim} = (g_0/\alpha_{ns})\varepsilon_s = 20–40$ mJ cm^{-2}, where $\varepsilon_s = 2$ mJ cm^{-2} is the saturation fluence and $g_0/\alpha_{ns} = 10–20$ is the ratio of the small-signal gain coefficient to the nonsaturable absorption coefficient [2]. This means that, under gain saturation conditions, filaments with $\varepsilon_f > \varepsilon_{lim}$ are absorbed by the gain medium of the amplifier and that, by contrast, the background radiation is amplified, leading to a more uniform energy distribution over the cross section of the beam. The nonlinear filament absorption and stimulated scattering give rise to additional losses in the windows of the amplifiers, which, together with the loss in the gain medium, limit the USP energy [38]. It is this circumstance that made it impossible to markedly raise the USP energy in the case of four-pass amplification in the preamplifier. Filaments developing during sequential passes were completely formed at the preamplifier output, so a filamented beam arrived at the input of the final amplifier [41]. For the same reason, we failed to compensate for the dispersion-induced pulse broadening in the amplification channel by using a negatively chirped input pulse. This reduced the amplified USP duration, but the output energy dropped sharply, making it impossible to raise the peak power. Moreover, the filament absorption in the windows of the amplifiers led to colour centre generation and a gradual reduction in transmission.

In the case of double-pass USP amplification in both amplifiers, filaments were completely formed a distance $L_f \approx 15$ m from the output of the final amplifier, which was roughly equal to the distance to the target chamber (Fig. 1).

Filamentation might then have a significant effect on the laser beam divergence and beam focusing onto a target. In particular, an important issue is phase relationships in a filament array. A random phase shift due to air turbulences or some other small-scale inhomogeneities in the amplification path may lead to phase mismatch between filaments and, as a consequence, to a considerable increase in beam divergence. In view of this, filamentation suppression and the effect of filamentation on the laser beam divergence (focusability) were the key issues addressed in this study.

3.2. Supercritical UV laser beam filamentation suppression in xenon

Beam filamentation and the associated energy loss and USP quality degradation can be avoided via amplification of frequency-chirped and stretched pulses and subsequent compression of the pulses to their original duration. Widely used in solid-state laser systems, this approach can be applied as well in KrF laser systems [43, 44]. However, because of the low saturation fluence in KrF amplifiers, and because a large laser beam cross section is necessary, large, expensive diffraction gratings are needed for the optical compressor. Moreover, available gratings have low reflectivity and low optical damage resistance in the UV spectral region.

In this study (see also Ref. [45]), Kerr defocusing of filaments in xenon is used to suppress the multiple filamentation of UV radiation. Xenon has an abnormally high negative nonlinear refractive index n_2^{Xe} at the KrF laser wavelength because of the two-photon resonance with the $6p[1/2]_0$ state [46]. At a xenon pressure $p = 1$ atm, its magnitude, $|n_2^{Xe}| = (963 \pm 112)\times10^{-24}$ m^2 W^{-1}, is almost one hundred times the nonlinear refractive index of atmospheric air: $n_2^{air} = (12 \pm 4)\times 10^{-24}$ m^2 W^{-1} [47]. This means that a xenon-filled cell can compensate for a positive phase shift accumulated in a long optical amplification path and during pulse delivery to the target chamber. To experimentally verify this assumption, we used a 2.5-m-long xenon-filled cell, in which the pressure was varied in the range 0.1 – 1.0 atm. The cell was placed various distances L from the final amplifier: where many filaments had already been formed ($L > L_f$) and where filamentation only began ($L < L_f$).

To visualise the UV laser beam at large differences between the filament and background radiation intensities, we used nonlinear fluorescence of K8 glass in the blue-green spectral region. The fluorescence of the narrow surface glass layer that absorbed the UV beam was imaged by an objective onto a Spiricon SP620U CCD beam profiler camera (Ophir Photonics). The calibration graph of glass fluorescence f against USP fluence ε was obtained in independent experiments on the Ti : sapphire front-end, whose 100-fs pulses were stretched to ~1-ps duration in a 20-cm-thick quartz layer and amplified by the discharge-pumped KrF laser. The energy of the amplified USPs was varied using a diffraction attenuator. The curve obtained can be represented by the power law function $f \propto \varepsilon^{0.4}$ in a wide range of ε values, differing by more than four orders of magnitude (Fig. 2). This allowed us to detect not only filaments but also (much weaker) background radiation in a single laser pulse without the beam profiler's CCD array saturation.

Figure 3 illustrates cross-sectional laser beam homogenisation a distance $L = 20$ m behind the final KrF amplifier. Without a cell, hundreds of filaments, with a characteristic diameter of ~300 μm, are seen in the beam cross section

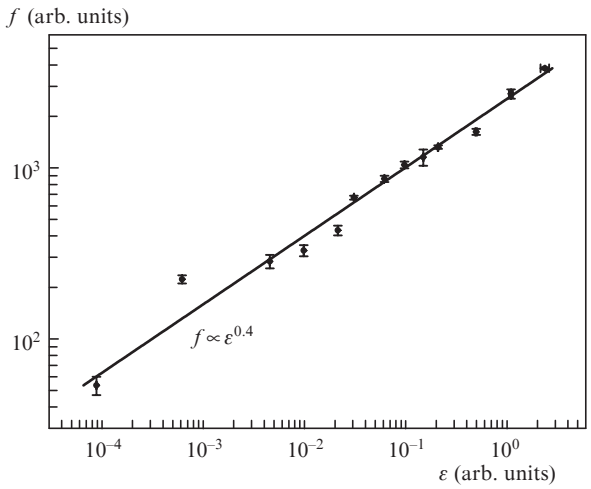

Figure 2. K8 glass fluorescence intensity as a function of fluence for 1-ps UV pulses.

(Fig. 3a). A cell filled with xenon at $p = 0.1$ atm ensures an almost complete filament defocusing, even though larger scale inhomogeneities in the beam intensity distribution persist (Fig. 3b). Concurrently, xenon ensures coherent conversion of the UV light into monochromatic IR radiation with a wavelength of 828 nm, corresponding to the $6p[1/2]_0 \rightarrow 6s[3/2]_1^0$ atomic transition. This radiation seems to be due to four-wave interaction and stimulated two-photon hyper-Raman scattering of UV light in xenon in the presence of two-photon resonance and ASE on this transition [48]. The characteristic near-field speckle pattern of the IR radiation and its near-field interference upon reflection from attenuation filters (Fig. 4a) attest to a coherent nature of this radiation, suggesting that the filaments in the UV laser beam are in phase and that the beam can be focused to a small spot size. When the IR radiation was focused by an $F = 17$ cm lens, many rings identical in diameter emerged in the far field, due to conical emission from the filaments at a cone angle of 8 mrad (Fig. 4b). The reason for the noncoincidince of the rings is that the bunch of filaments in the weakly convergent laser beam behind the final amplifier also converged at a small angle.

Placing a xenon-filled cell 5 m away from the final amplifier, where multiple filamentation only began, prevented beam filamentation over distances up to 50 m from the final

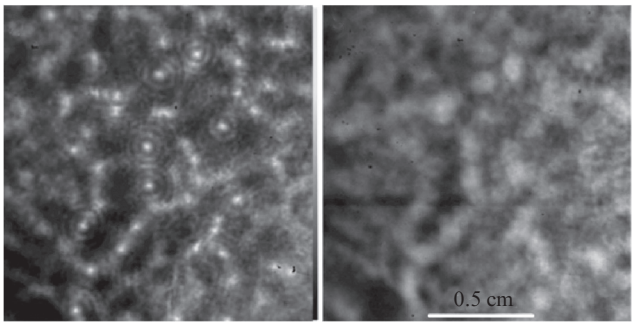

Figure 3. Portions of a cross section of (a) the laser beam with a filament array and (b) the beam passed through a cell filled with xenon at a pressure of 0.1 atm.

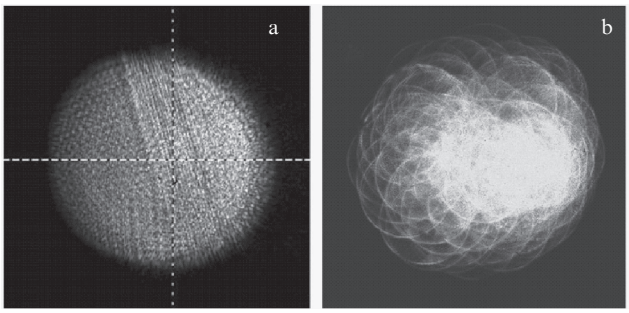

Figure 4. (a) Near- and (b) far-field IR intensity distributions for the conical emission from filaments.

amplifier. Those experiments were described in greater detail elsewhere [45]. Calorimetry data showed that, at a xenon pressure in the cell $p = 1$ atm, it absorbed less than 20% of the USP energy and only a small part of the absorbed radiation was converted into IR radiation.

3.3. Effect of filamentation on the laser beam divergence

In these experiments, we used a 1-m-long cell filled with xenon to a pressure $p = 1$ atm, which was placed 5 m away from the final amplifier (Fig. 1). The angular intensity distribution of the UV laser beam passed through the cell or without a cell was measured directly at the inlet of the target chamber, where we placed an $F = 2.5$ m long-focus spherical mirror, with the glass-plate UV converter located in its focal plane. Using a wedge, about 4% of the USP energy was directed to the plate. The converter fluorescence was imaged onto the beam profiler camera. Neutral optical filters mounted on the beam profiler served to attenuate fluorescence when the focal spot was imaged onto the CCD array (Fig. 5). The images obtained at various attenuations allow one to see both the central part of the intensity distribution (Fig. 5c) and its far periphery (Figs 5a, 5b) (in such cases, the central part was in saturation). In the case of the laser beam passed through the xenon-filled cell, interference fringes in the peripheral parts of the beam spot were due to diffraction from the aperture of the cell. Figure 5d shows the horizontal fluorescence intensity profile across the focal spot. The profile was obtained by joining numerical values from the CCD array for the three distributions at different attenuations.

An analogous intensity profile was obtained for the laser beam with a filament array when there was no cell. To take into account the slight astigmatism introduced by the measurement system, the fluorescence profiles were averaged in two mutually perpendicular directions. Next, using the calibration graph of converter fluorescence against UV fluence, $f \propto \varepsilon^{0.4}$, we calculated the angular distribution of the laser beam intensity, varying it over eight orders of magnitude. Integrating the resultant distribution, we found the fraction of optical energy at a given angle (Fig. 6). The laser beam divergence at the 10% intensity level was 0.14 mrad. This angle accounted for 50% of the pulse energy. Without a cell, the filamented beam divergence was higher by just 15% to 20%. Thus, laser beam divergence was determined not so much by filamentation (because the entire filament array was in phase) as by the accuracy in the fabrication of the large-scale optics for the KrF amplifiers and other optical components of the section responsible for beam amplification and delivery to the target chamber.

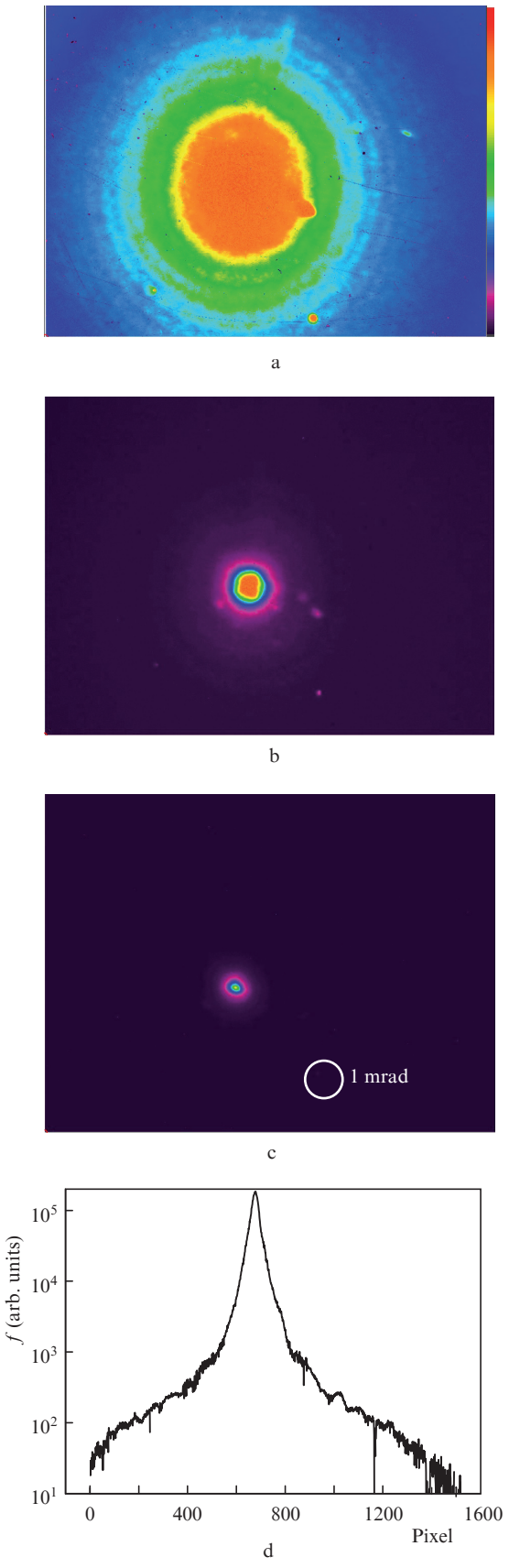

Figure 5. (Colour online) Beam profiler images of the focal spot of a laser beam passed through a xenon-filled cell: (a) no attenuation, (b) 3% and (c) 0.4% attenuation of glass UV converter fluorescence; (d) horizontal fluorescence profile obtained by joining the distributions in Figs 5a–5c.

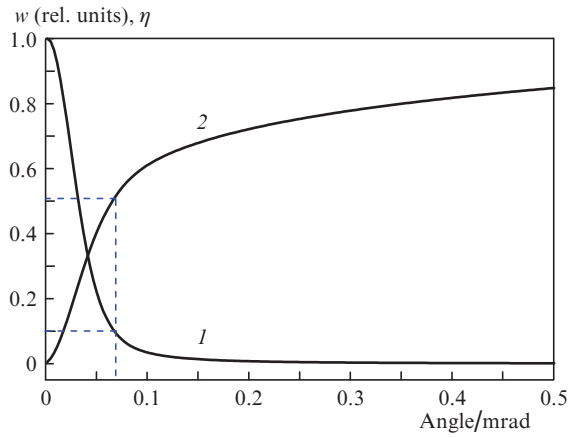

Figure 6. (*1*) Angular UV fluence w distribution of the beam passed through a xenon-filled cell and (*2*) fraction of energy η at a given angle.

4. Experiments on the interaction of UV USPs with targets

4.1. Crater shape and laser beam intensity distribution in the focal spot

In the first test experiments using four-pass USP amplification in the preamplifier and double-pass amplification in the final amplifier, the USP energy at the inlet of the target chamber did not exceed 125 mJ because of the high loss due to laser beam filamentation (see Section 3.1). The beam had a diameter of 120 mm at the chamber inlet and was focused onto a target by an $F = 400$ mm spherical mirror. Our estimates suggest that such a mirror produces considerable spherical aberrations, which lead to an increase in focal spot diameter to ~300 μm. We irradiated various targets made of Teflon, copper and poly(methyl methacrylate) (organic glass), as well as 20-μm-thick single-walled carbon nanotube (SWCNT) films produced by the arc-discharge method and supported on copper* [49]. The targets were secured to a micro-adjustable suspension in a vacuum chamber, which was pumped down to ~10^{-5} mbar. A low-density (30–50 mg cm^{-3}) SWCNT layer is of interest for charged particle acceleration [37], because the electron density in a fully ionised plasma of this material is of the same order as the critical electron density for UV laser light.

The organic glass target was used to evaluate the crater diameter and depth, which were measured on a microscope by adjusting the depth of focus to the target surface or crater bottom (Fig. 7). The craters had a symmetrical shape, with a central round hole surrounded by a halo due to wings of the intensity distribution over the focal spot. The ablation of organic glass is distinct in that, at the relatively large penetration depth of UV light (~6 μm), it causes photochemical decomposition into lighter fragments, which requires less energy than does vaporisation [50]. At low UV fluences ($\varepsilon \leqslant 1$ J cm^{-2}), the thickness of the removed layer (etch depth) was observed to scale logarithmically with fluence, i.e. the etch depth (a few microns) was smaller than the penetration depth of UV light in the organic glass. In our case, at high UV fluences in the centre of the beam spot, the crater depth l was a linear function of USP energy (Fig. 8a), which allows us to find the mass of material removed per unit area of the target, $m = \rho l$ (where $\rho = 1.2$ g cm^{-3} is the density of organic glass) and relate it to the UV fluence in the centre of the focal point. This quantity can be found by analysing the cross-sectional size of ablation craters as a function of USP energy.

It is reasonable to assume that, at various USP energies E, e.g. at the highest energy in a given series of measurements, E_{max}, and at any other, the respective crater radii r_{max} and r correspond to the same 'threshold' fluence at which target ablation begins. For a Gaussian fluence distribution in the focal spot, $\varepsilon(r) = \varepsilon_0 \exp[-(r/a)^2]$, where $\varepsilon_0 = E/(\pi a^2)$ is the fluence in the centre of the spot, we obtain the relation $r_{max}^2 - r^2 = a^2 \ln(E_{max}/E)$. The characteristic radius of the Gaussian distribution, a, can then be found from the slope of the graph of $r_{max}^2 - r^2$ against $\ln(E_{max}/E)$. Analysis of the measured crater size as a function of pulse energy (Fig. 8b) indicates that there are two regions differing in the slope of the graph, i.e. the fluence distribution in the focal spot can be represented as a combination of two Gaussians. The central part of the distribution, with $r \leqslant 40$ μm, has a characteristic radius $a_1 \approx 22$ μm. It accounts for 65% of the pulse energy. The rest of the energy is accounted for by wings of the distribution, with a characteristic radius $a_2 \approx 66$ μm. Comparison with more accurate beam divergence measurements (see Section 3.3) shows, however, that the fraction of the pulse

*The SWCNT films were grown and provided for our experiments by E.D. Obraztsova (A.M. Prokhorov General Physics Institute, Russian Academy of Sciences).

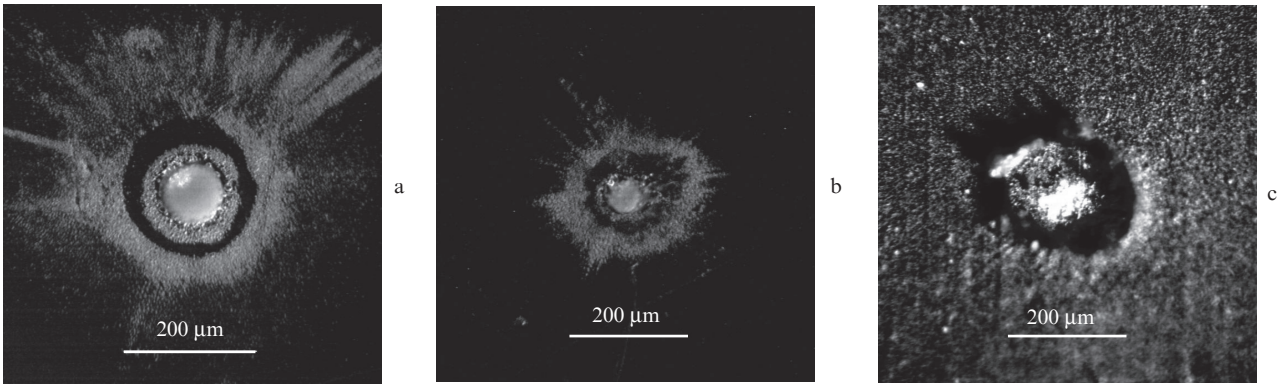

Figure 7. Images of ablation craters produced in (a, b) organic glass and (c) a SWCNT film at USP energies E = (a, c) 60 and (b) 13 mJ.

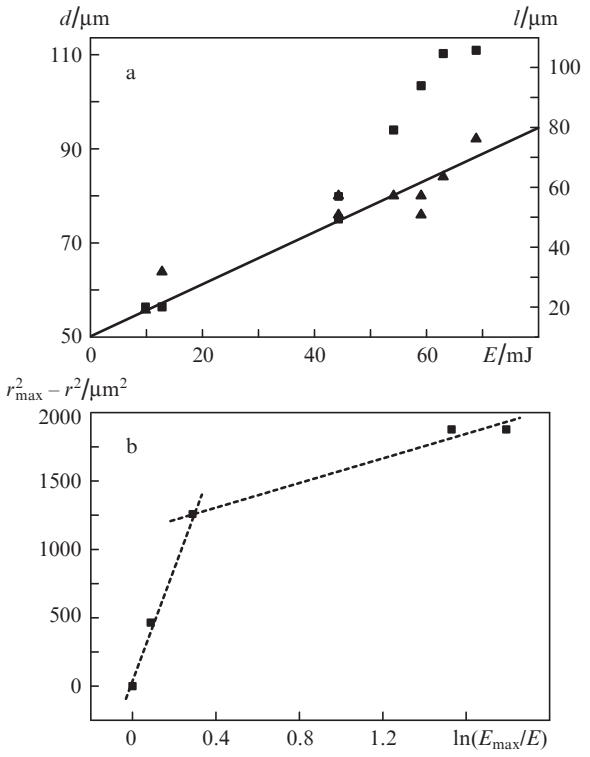

Figure 8. (a) Effect of USP energy E on the diameter d (■) and depth l (▲) of the central hole of ablation craters in organic glass; (b) $r^2_{max} - r^2$ as a function of $\ln(E_{max}/E)$.

energy density in the wings of the distribution is somewhat larger than that derived from analysis of the crater size. Nevertheless, the data in Fig. 8 can be used to evaluate the energy consumption for the ablation of organic glass by picosecond pulses. At high fluences (several kJ cm^{-2}), it was $\sim 3.6\times10^5$ J g^{-1}, which is two orders of magnitude higher than that measured for nanosecond pulses at low fluences [50]. The difference is obviously caused by the energy consumption for the ionisation of the target material and heating of the plasma.

In the next series of experiments, with double-pass USP amplification in both KrF amplifier stages and multiple laser beam filamentation suppression in a xenon-filled cell (Fig. 1), the USP energy at the inlet of the target chamber increased to 250 mJ. The ASE energy in a solid angle of $\sim 2\times10^{-5}$ sr was ~3% of the USP energy, which was consistent with the measured angular distribution of the ASE intensity [2]. Using the measured laser beam divergence (0.14 mrad) and taking into account the relationship between the solid angles involved, we can estimate the USP contrast relative to ASE in the case of focusing onto a target: $C_\varepsilon \approx 3\times10^5$ for the fluence ratio and $C_I \approx 3\times10^{10}$ for intensities.

The laser beam was focused onto a target by an F = 300 mm parabolic mirror. Before mounting it in the target chamber, using the beam profiler we measured the focal spot size of the front-end beam, which had passed the entire optical path, without pumping the amplifiers (Fig. 9). The measurement results show that the spot diameter at the 10% intensity level is ~75 μm, which is twice the value expected from the measured laser beam divergence (see Section 3.3) and suggests that the parabolic mirror had insufficient quality.

The USP duration at the target chamber inlet was measured in preliminary experiments using a specially designed single-shot autocorrelator based on three-photon fluores-

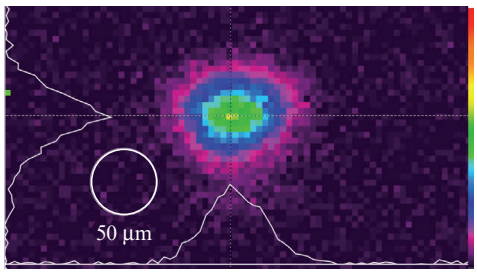

Figure 9. (Colour online) Image of the focal spot of front-end USPs that passed through the amplifiers without pumping and were focused onto the beam profiler by an F = 0.3 m parabolic mirror.

cence excitation on the C → A transition of the XeF excimer molecule [51]. The pulse duration thus found, ~1 ps, coincides with that measured previously using an electron-optical camera and with a value calculated with allowance for the dispersion-induced USP broadening in the optical section between the front-end and target chamber [39]. Thus, the highest intensity in the centre of the focal spot in our experiments on USP–target interaction was $\sim 10^{16}$ W cm^{-2}.

4.2. Bremsstrahlung X-ray measurements and estimation of the electron temperature of a laser plasma

To find the electron temperature of a laser plasma produced by irradiating hard and low-density nanocarbon targets, we used a method based on measurements of bremsstrahlung X-rays that passed through various absorbers [52]. The absorbers used in our experiments were aluminium foils 20, 40, 80 and 160 μm thick, which were mounted together with a 5-μm-thick protective mylar polymer film. A micron-thick layer of aluminium sputter-deposited on the film reflected visible light emitted by the laser plasma. The X-rays transmitted through the absorbers were converted to the visible range by a plastic scintillator and detected by a pulsed photomultiplier tube with a time resolution of a few nanoseconds. For the photomultiplier to operate in a linear mode, neutral optical filters were mounted behind the scintillator.

X-ray pulses with a sufficiently large amplitude were reliably detected only behind the mylar film and 20-μm-thick aluminium foil (Fig. 10). Figure 11a shows the transmission of the absorbers as a function of X-ray photon energy (data taken from X-ray tables [53]). Both absorbers transmit only

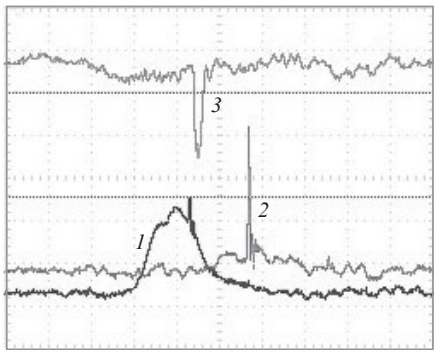

Figure 10. Oscilloscope traces of (*1*) ASE and USPs behind the preamplifier, (*2*) USPs behind the final amplifier and (*3*) an X-ray pulse emitted by a plasma. Time base, 50 ns div^{-1}.

photons with energies above 1 keV. As shown in previous experiments [15, 24, 26], the main contribution to the emission spectrum of a dense laser plasma in this region is made by bremsstrahlung X-rays. In the case of a nanocarbon target, the ratio of the X-ray signal amplitudes behind the mylar and aluminium films was 25 : 1. Assuming a Maxwellian distribution of electrons in the plasma, we calculated the bremsstrahlung X-ray spectra behind the absorbers (Fig. 11b). The ratio of the area under the spectra coincided with the measured signal ratio at a plasma electron temperature $T_e \approx$ 850 eV. The absence of X-ray pulses in the case of thicker aluminium filters strongly suggests that the laser plasma formed from the low-density nanocarbon target contains no fast, epithermal electrons. In addition, similar results were obtained for the copper target. Clearly, intensities exceeding those reached in experiments are needed to accelerate electrons in a low-density plasma. However, measurement results might be influenced by the fact that a hot dense plasma exists for no longer than tens of picoseconds [14, 15], whereas the technique used here integrated the X-ray energy over several nanoseconds.

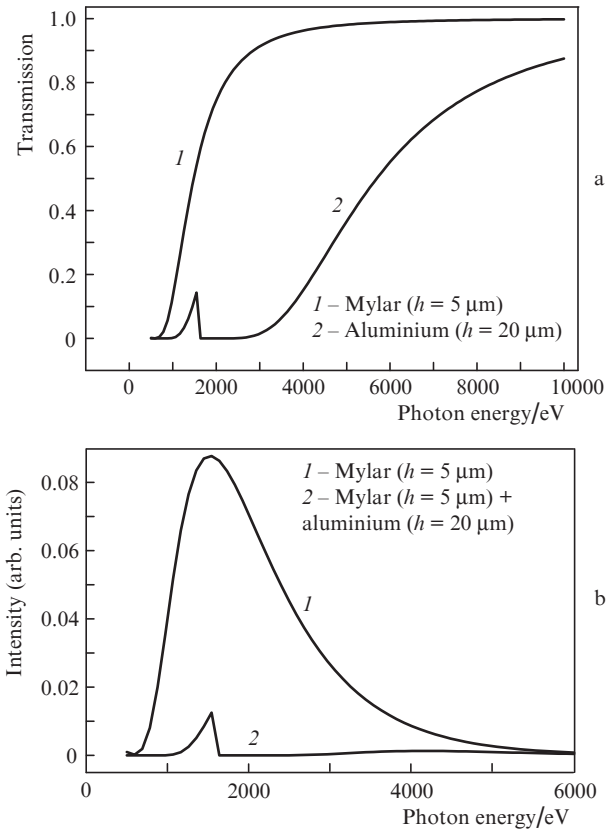

Figure 11. (a) Transmission of the mylar and aluminium filters and (b) bremsstrahlung X-ray spectra behind the filters. The plasma electron temperature is 850 eV; h is the filter thickness.

5. Conclusions

For experiments on the interaction of UV light with targets at the GARPUN MTW terawatt laser facility, we chose a double-pass amplification of 100-fs pulses from the Ti : sapphire front-end in two electron beam-pumped large-aperture KrF amplifier stages, which ensured 0.25 J of energy on a target at a maximum USP contrast relative to ASE $C_\varepsilon \approx 3\times10^5$ and $C_I \approx 3\times10^{10}$, a laser beam divergence of 0.14 mrad (at the 10% intensity level) and a pulse duration of ~1 ps. When the laser beam was focused by an $F = 0.3$ m parabolic mirror, the intensity incident on the targets was $\sim10^{16}$ W cm^{-2}.

A xenon-filled cell was used to suppress multiple laser beam filamentation, which restricts the limiting pulse energy and pulse duration and influences the beam divergence and beam focusing onto a target. Owing to the two-photon resonance of KrF laser light with the $6p[1/2]_0$ atomic state, the negative nonlinear refractive index of xenon led to the Kerr defocusing of high-intensity filaments and prevented beam filamentation over a 50-m-long air path. We observed monochromatic conical emission from filaments in xenon at a wavelength of 828 nm with a cone angle of ~8 mrad. The coherent conversion of UV light into IR radiation indicates that the filaments in the laser beam were in phase.

A technique was developed for detecting bremsstrahlung X-rays of a laser plasma using a plastic scintillator and a photomultiplier tube with a nanosecond time resolution. Using X-ray attenuators, we measured the plasma electron temperature, which was found to be 850 eV for copper targets and a low-density single-walled carbon nanotube target.

It is worth noting that it is possible to raise the intensity incident on targets by one to two orders of magnitude in subsequent experiments owing to the self-compression of negatively chirped pulses, laser beam filamentation suppression in xenon and the use of more perfect short-focus parabolic optics for laser beam focusing.

Acknowledgements. We are grateful to V.Yu. Bychenkov for initiating and supporting this study.

This work was supported by the Russian Science Foundation (Grant No. 14-12-00194, Experimental Studies of the Feasibility of Particle Acceleration from Low-Density Targets by UV Laser Pulses), the Russian Foundation for Basic Research (Grant No. 15-02-09410) and the International Atomic Energy Agency (Contract No. 19 273, Investigation of Intense UV Laser Beam Propagation and Delivery).

References

1. Danson C., Hillier D., et al. *High Power Laser Sci. Eng*., **3**, e3 (2015).
2. Zvorykin V.D., Didenko N.V., Ionin A.A., et al. *Laser Part. Beams*, **25**, 435 (2007).
3. Foldes I.B., Szatmari S. *Laser Part. Beams*, **26**, 575 (2008).
4. Divall E.J., Edwards C.B., Hirst G.J., et al. *J. Mod. Opt*., **43**, 1025 (1996).
5. Shaw M.J., Ross I.N., Hooker C.J., et al. *Fusion Eng. Des*., **44**, 209 (1999).
6. Owadano Y., Okuda I., Matsushima I., et al., in *Inertial Fusion Sciences and Applications 2001* (Amsterdam: Elsevier, 2001) pp 465–469.
7. Luk T.S., McPherson A., Gibson G., et al. *Opt. Lett*., **14**, 1113 (1989).
8. McIntyre I.A., Rhodes C.K. *J. Appl. Phys*., **69**, R1 (1991).
9. Mizoguchi M., Kondo K., Watanabe S. *J. Opt. Soc. Am. B*, **9**, 562 (1992).
10. Bouma B., Luk T.S., Boyer K., Rhodes C.K. *J. Opt. Soc. Am. B*, **10**, 1180 (1993).
11. Szatmari S., Almasi G., Feuerhake M., Simon P. *Appl. Phys. B*, **63**, 463 (1996).
12. Omenetto F.G., Boyer K., Longworth J.W., et al. *Appl. Phys.*, **64**, 643 (1997).
13. Bekesi J., Szatmari S., et al. *Appl. Phys. B*, **75**, 521 (2002).
14. Cobble J.A., Kyrala G.A., Hauer A.A., et al. *Phys. Rev. A*, **39**, 454 (1989).
15. Smith R.A., Barrow V., et al. *Appl. Phys. B*, **50**, 187 (1990).

16. Barrow V., Willi O., et al. *Appl. Phys. Lett*., **57**, 2086 (1990).
17. Lee P.H.J., Casperson D.E., Schappert G.T., Olson G.L. *J. Opt. Soc. Am. B*, **7**, 272 (1990).
18. Fedosejevs R., Ottman R., Sigel R., et al. *Appl. Phys. B*, **50**, 79 (1990).
19. Zigler A., Burkhalter P.G., Nagel D.J., et al. *Opt. Lett.*, **16**, 1261 (1991).
20. Tallents G.J., Key M.H., Norreys P., et al. *Opt. Commun*., **89**, 410 (1992).
21. Li Y.M., Broughton J.N., Fedosejevs R. *Opt. Commun*., **93**, 366 (1992).
22. Turcu I.C.E., Ross I.N., Tallents G.J. *Appl. Phys. Lett*., **63**, 3046 (1993).
23. Casperson D.E., Cobble J.A., Fulton R.D., et al. *J. Appl. Phys*., **74**, 3707 (1993).
24. Brougton J.N., Fedosejevs R. *J. Appl. Phys*., **74**, 3712 (1993).
25. Sauerbrey R., Fure J., Le Blanc S.P., et al. *Phys. Plasmas*, **1**, 1635 (1994).
26. Teubner U., Wulker C., Theobald W., Forster E. *Phys. Plasmas*, **2**, 972 (1995).
27. Blyth W.J., Preston S.G., Offenberger A.A., et al. *Phys. Rev. Lett*., **74**, 554 (1995).
28. McPherson A., Borisov A.B., Boyer K., Rhodes C.K. *J. Phys. B: At. Mol. Opt. Phys*., **29**, L291 (1996).
29. Teubner U., Gibbon P., Forster E., et al. *Phys. Plasmas*, **3**, 2679 (1996).
30. Wulker C., Theobald W., Gnass D.R., et al. *Appl. Phys. Lett*., **68**, 1338 (1996).
31. Tao Y.Z., Wang N.Y., Shan Y.S., et al. *Laser Part. Beams*, **20**, 129 (2002).
32. Ryc L., Barna A., Calcagno L., et al. *Phys. Scr*., **T161**, 014032 (2014).
33. Heissler P., Barna A., Mikhailova J.M., et al. *Appl. Phys. B*, **118**, 195 (2015).
34. Bodner S., Schmitt A.J., Sethian J.D. *High Power Laser Sci. Eng*., **1**, 2 (2013).
35. Ewing J.J., Haas R.A., Swingle J.C., et al. *IEEE J. Quantum Electron.*, **QE-15**, 368 (1979).
36. Zvorykin V.D., Lebo I.G., Rozanov V.B. *Kratk. Soobshch. Fiz*., Nos 9–10, 20 (1997).
37. Bychenkov V.Yu., Brantov A.V., Govras E.A., Kovalev V.F. *Usp. Fiz. Nauk*, **185**, 77 (2015).
38. Zvorykin V.D., Ionin A.A., Levchenko A.O., et al. *Quantum Electron*., **44**, 431 (2014) [*Kvantovaya Elektron*., **44**, 431 (2014)].
39. Zvorykin V.D., Levchenko A.O., Ustinovskii N.N. *Quantum Electron*., **40**, 381 (2010) [*Kvantovaya Elektron*., **40**, 381 (2010)].
40. Zvorykin V.D., Ionin A.A., Levchenko A.O., et al. *Quantum Electron*., **43**, 332 (2013) [*Kvantovaya Elektron*., **43**, 332 (2013)].
41. Zvorykin V.D., Ionin A.A., Levchenko A.O., et al. *Nucl. Instrum. Methods Phys. Res., Sect. B*, **355**, 227 (2015).
42. Smetanin I.V., Levchenko A.O., Shutov A.V., et al. *Nucl. Instrum. Methods Phys. Res., Sect. B*, **369**, 87 (2016).
43. Houliston J.R., Ross I.N., Key M.H., et al. *Opt. Commun*., **104**, 350 (1994).
44. Ross I.N., Damerell A.R., Divall E.J., et al. *Opt. Commun*., **109**, 288 (1994).
45. Zvorykin V.D., Goncharov S.A., Ionin A.A., et al. *Laser Phys. Lett*., **13**, 125404 (2016).
46. Lehmberg R.H., Pawley C.J., Deniz A.V., et al. *Opt. Commun.*, **121**, 78 (1995).
47. Shaw M.J., Hooker C.J., Wilson D.C. *Opt*. *Commun*., **103**, 153 (1993).
48. Tunnermann A., Mossavi K., Wellegehausen B. *Phys. Rev. A*, **46**, 2707 (1992).
49. Obraztsova E. *Fotonika*, (4), 84 (2015).
50. Srinivasan R., Braren B., Dreyfus R.W., et al. *J. Opt. Soc. Am. B*, **3**, 785 (1986).
51. Sarakura N., Watanabe M., Endoh A., Watanabe S. *Opt. Lett.*, **13**, 996 (1988).
52. Basov N.G., Zakharenkov Yu.A., Rupasov A.A., et al. *Diagnostika plotnoi plazmy* (Dense Plasma Diagnostics) (Moscow: Nauka, 1989) p. 124.
53. X-Ray Tables; http://henke.lbl.gov.